In-situ growth of metallic nanoparticles on perovskite parent as a hydrogen electrode for solid oxide cells

Yao Wang[a],Xueling Lei[b], Yanxiang Zhang[c], Fanglin Chen*[d], Tong Liu*[a,e]

[a] Key Laboratory of Hydraulic Machinery Transients (Wuhan University), Ministry of Education, School of Power and Mechanical Engineering, Wuhan University, Wuhan, Hubei 430072, China

[b] Department of Physics, Jiangxi Normal University, Nanchang, Jiangxi 330022, China

[c] National Key Laboratory for Precision Hot Processing of Metals, School of Materials Science and Engineering, Harbin Institute of Technology, Harbin 150001, China

[d] Department of Mechanical Engineering, University of South Carolina, Columbia, SC 29208, USA

[e] Suzhou Institute of Wuhan University, Suzhou, Jiangsu 215123, China

Corresponding Authors

*E-mail: liu_tong@whu.edu.cn (T. Liu.) and chenfa@cec.sc.edu (F. Chen)

Abstract

In this work, *in-situ* fabricated nano-socketed Fe-Ni particles structured $Sr_2Fe_{1.5}Mo_{0.5}O_{6-\delta}$ (SFM) electrodes are proposed to simultaneously combine good electrochemical properties of Ni-based materials and good stabilities of SFM-based materials. Preliminary studies on the Ellingham diagram and density functional theory offer certain theoretical basis for realizing the feasibility to extract Fe-Ni alloy from parent $Sr_2Fe_{1.3}Ni_{0.2}Mo_{0.5}O_{6-\delta}$ in the viewpoint of thermodynamic and minimum energy principle. Experimental results according to X-ray diffraction, scanning electron microscopy-elements mapping, high resolution transmission electron microscopy measurements show that a large amount of uniformly dispersed Fe-Ni nano-catalysts are elegantly exsolved from

the perovskite oxide parent. Electrical conductivity relaxation results indicate that surface exchange coefficient of SFM-based material is enhanced from 0.5×10^{-3} to 1.7×10^{-3} cms^{-1} by the in-situ growth of Fe-Ni alloy at 800 ^{o}C. The in-situ fabricated Fe-Ni@SFM combined with $Ce_{0.8}Sm_{0.2}O_{1.9}$ (SDC) composite electrodes perform a considerably high electrolysis current density of 1257 mA cm^{-2} at 1.3 V, 850 ^{o}C and polarization resistance of 0.20 Ωcm^2 at open circuit voltage and 850 ^{o}C. Distribution relaxation of time analysis of impedance spectra shows that the gas conversion process is the rate-limiting step in the Fe-Ni@SFM-SDC hydrogen electrode for steam electrolysis.

Keywords: *In-situ* exsolution, Hydrogen electrode, Solid oxide cell, Steam electrolysis, Perovskite

1. Introduction

Hydrogen is a clean energy carrier with abundant resource, which has been considered as one of the most attractive future energy alternatives to fossil fuel. Compared to the conventional methods to produce hydrogen such as methane reforming, coal gasification and so on, water electrolysis is probably the cleanest method to produce hydrogen with high purity[1-3]. It has a lot of advantages to perform the steam electrolysis process at high operating temperature using the solid oxide electrolysis cells (SOECs). According to the thermodynamic analysis for water splitting reaction, with the operating temperature increasing from 200 to 1000 °C, the ratio of electrical energy to total energy input has decreased from 90% to 70%, indicating that about 20% energy could be supplied with industrial waste heat instead of electricity[3]. As a result, it is more cost and energy efficient to perform the water electrolysis process at high temperature using SOEC. Secondly, high temperature SOEC can perform a faster electrode reaction kinetics due to its lower electrode polarization resistance.

In recent years, solid oxide cells (SOCs) using the conventional Ni-based materials as the hydrogen electrode has been intensively studied. The Ni-based cermets have exhibited excellent electrochemical properties. However, they are susceptible to degrade at high operating temperature or other tough conditions including thermal/redox cycling or in presence of hydrocarbon or hydrogen sulfide (H_2S)[4]. Since Ni has a relatively low melting point, their grains could agglomerate to break the contact of Ni particles with ceramic components or other Ni grains, leading to a reduction of electrode conductivity and effective three-phase boundaries (TPBs), and further resulting in an increase of both ohmic resistance and electrode polarization resistance. Consequently, a variety of perovskite oxides such as $La_{0.75}Sr_{0.25}Cr_{0.5}Mn_{0.5}O_3$ (LSCM), $Sr_2Fe_{1.5}Mo_{0.5}O_6$ (SFM),

$La_{0.3}Sr_{0.7}TiO_{3+\delta}$ (LST) have been developed as alternative candidates for Ni-cermets because of their good structural stability and flexible mixed conductivity[5-12]. However, in some cases these Ni-free ceramic hydrogen electrodes exhibit inadequate catalytic activity for steam splitting reaction. To simultaneously enhance the electrochemical properties and stabilities of SOCs, previous studies demonstrate that a number of easily reducible and catalytically active cations (such as Ni^{2+}, Co^{2+}, Pd^{4+}, Ru^{2+}, Cu^{2+}, etc.) can be substituted on the B-sites of perovskite oxide in oxidizing conditions, and then partially *in-situ* exsolved out of the matrix lattice as active nano-catalysts in a reducing atmosphere[13-23]. This kind of self-regenerative property of perovskite oxides offer a more time- and cost-effective strategy to produce fine and uniformly distributed nano-catalysts, which provide more active sites and larger specific surface areas to facilitate catalytic reactions during the chemical and energy conversion process[13, 15, 24, 25]. Moreover, the nano-socketed catalyst particles are observed to be more resilient to grains coarsening, coking, redox and H_2S poisoning. For instance, Neagu *et al.* have elegantly fabricated nano-socketed nickel particles from A-site deficient $(La_{0.52}Sr_{0.28})(Ni_{0.06}Ti_{0.94})O_3$ perovskite by in-situ exsolution[22]. These exsolved Ni particles pinned into parent grains with a depth of ~20 nm had a strong particle-substrate interaction, resulting in lower tendency to grains coarsening, and consequently better thermal stability at 900 °C. The strong catalyst-support interface was also effective to prevent carbon growth, and methane reforming test on $(La_{0.52}Sr_{0.28})(Ni_{0.06}Ti_{0.94})O_3$ perovskite powders with exsolved Ni particles exhibited remarkably low extent of coking[22]. Sun *et al.* have reported an in-situ fabricated Ni nanoparticles structured $La_{0.7}Sr_{0.3}Cr_{0.85}Ni_{0.15}O_3$ anode for solid oxide fuel cell (SOFC) application[26], which showed an improved and stable electrochemical performance with a maximum power density of 460 $mWcm^{-2}$ in 5000 ppm H_2S-H_2 fuel at 800 °C. The nano-sized Ni particles had less dimensional change during

the redox cycles, reasonably leading to a good structural redox stability of the electrodes. Additionally, the cell performance were fully recovered during the 4-redox-cycle measurement without obvious degradation in the maximum power density[26]. Yang *et al.* have reported an in-situ fabricated Co-Fe nanoparticles structured $(Pr_{0.4}Sr_{0.6})_3(Fe_{0.85}Ni_{0.15})_2O_7$ composite as anode for SOFC application[27], which exhibited a high maximum power density of 0.92 Wcm^{-2} in 3 vol.% H_2O humidified C_3H_8 atmosphere at 850 ^oC. The cell performance was stable in more than 100 h test, and negligible carbon signal was detected in the Raman spectra for as-tested anode[27]. Although the in-situ exsolution method becomes more and more popular to fabricate nano-structured electrode, it is still not yet very clear the theoretical basis to extract metals from the oxide. Xiao and Gao *et al*. have calculated the Gibbs free energy change[18, 28], ΔG, of metal formation ($1/x\ M_xO_y + y/x\ H_2(g) = M + y/x\ H_2O(g)$, M = Ni, Co, Mo, Sr, La, etc) from its oxide at different operating temperatures, which is usually used to evaluate the ease of reduction of metal oxides and temperature dependence of the stability for compounds. However, the analysis of ΔG does not consider the effect of reducing atmosphere, which would certainly influence the exsolved particle size, phase structure and further electrochemical performance of in-situ fabricated nano-structured electrode.

In this work, a stable and well conductive perovskite oxide $Sr_2Fe_{1.3}Ni_{0.2}Mo_{0.5}O_{6-\delta}$ (SFMNi) is chosen as the parent material, from which catalytically active Fe-Ni alloy nanoparticles are exsolved and uniformly pinned into the perovskite oxide matrix to comprise a highly-performed nano-structured electrode for SOC application. The Ellingham diagram and density functional of theory (DFT) are used to evaluate the ceramic oxide stability to study the thermodynamic feasibilities for producing metallic particles, while X-ray diffraction (XRD), scanning electron microscopy (SEM)

equipped with energy dispersive X-ray spectrometers (EDS) system, high-resolution transmission electron microscopy (HRTEM), and electrical conductivity relaxation (ECR) measurements were applied to study the phase structure and conductive properties of in-situ Fe-Ni alloy structured SFMNi perovskite oxide (Fe-Ni@SFM). The electrochemical performance of the SOCs with Fe-Ni@SFM composite powders as hydrogen electrode materials are also investigated by recording the current density-cell voltage (*i-V*) data and electrochemical impedance spectra (EIS) of the cells.

2. Experimental Section

2.1 Preparation of characterization of electrode powders

$Sr_2Fe_{1.3}Ni_{0.2}Mo_{0.5}O_{6-\delta}$ (SFMNi) materials were synthesized by using a glycine and citric acid assisted combustion method[13]. Stoichiometric amount of $Sr(NO_3)_2$, $Fe(NO_3)_3 \cdot 9H_2O$, $(NH_4)_6Mo_7O_{24} \cdot 4H_2O$ and $Ni(NO_3)_2 \cdot 6H_2O$ were dissolved in the deionized water under continuous stirring, and citric acid and glycine were then added as the combustion-assisting chemicals and chelating agent at the molar ratio of citric acid: glycine: perovskite oxide=0.95:10:1. Subsequently, the solution was heated on a hot plate until the self-combustion occurred. The raw powders of SFMNi materials were grinded and fired at 1050 ºC for 5h in air to completely remove the organic residues. Metallic Fe-Ni particles were formed by reducing the SFMNi powders at 800 ºC in 3 vol% H_2O humidified H_2 atmosphere. Other powders including $Ce_{0.9}Gd_{0.1}O_{1.95}$ (GDC), $La_{0.5}Ce_{0.5}O_{1.8}$ (LDC), $Sm_{0.2}Ce_{0.8}O_{1.9}$ (SDC), and $La_{0.6}Sr_{0.4}Co_{0.2}Fe_{0.8}O_{3-\delta}$ (LSCF) were also prepared using the similar method, while $La_{0.8}Sr_{0.2}Ga_{0.87}Mg_{0.13}O_3$ (LSGM) powders were purchased from FuelCellMaterials Inc.

The SFMNi powders were mixed together with GDC powders at a weight ratio of 1:1 to obtain

SFMNi-GDC composite powders, and then the composite powders were pressed into a rectangular bar (40 × 6 × 1 mm^3), and sintered to be dense at 1300 °C for electrical conductivity and ECR measurements. Four platinum wires were attached to the sintered bar sample as the probes, platinum paste were printed onto the wires and sintered at 800 °C to improve their contact to the bars. The sample with well-attached Pt wires was placed in a tubular furnace with flowing H_2 (3 vol% H_2O) at a rate of 40 mL min^{-1}. The electrical conductivities of the reduced SFMNi-GDC bars at the temperature range from 800 to 400°C were recorded by a multimeter (Keithley model 2001). The oxygen surface exchange coefficient, k_{chem}, and oxygen ion diffusion coefficient , D_{chem}, were calculated by fitting the normalized conductivity as a function of elapsed time over the surrounding atmosphere switching from 33%CO_2-67%CO to 50%CO_2-50%CO at a flow rate of 200 mL min^{-1}. The fitting calculation was performed at stepwise intervals over a range of D and k to get minimum discrepancy between the calculated and measured results using Matlab software[29, 30].

2.2 Fabrication of electrolyte-supported single cells

Electrolyte-supported single cells consisted of SFMNi-SDC cathode, LDC interlayer, LSGM electrolyte and SDC-LSCF anode are fabricated to perform high temperature steam electrolysis process for H_2 production. The LSGM electrolyte pellets with a diameter of 13 mm were pressed and sintered to be dense at 1400 °C. Following, the LDC slurry was dip-coating on one side of the dense LSGM electrolyte and sintered at 1200 °C to form a thin interlayer between the electrolyte and cathode to avoid the inter-reaction between the Ni element with LSGM. The SFMNi-SDC ink was prepared by mixing SFMNi powders with SDC powders at a weight ratio of 60:40 with a binder (Heraeus V006), and screen-printed onto the surface of the LDC interlayer. Similarly, the SDC-LSCF ink at a weight ratio of 50 to 50 was prepared and screen-printed onto the other side of the

LSGM electrolyte. Both the SFMNi-SDC hydrogen electrode and the SDC-LSCF oxygen electrode were co-fired at 1100 ^{o}C for 2 hours. The effect area of the oxygen electrode was 0.33 cm^2. Gold (Au) paste was used as the current collector, which was pre-fired at 800 ^{o}C for 1 hour.

2.3 Characterization

Single cells were sealed onto an alumina tube with a conducting paste and ceramic adhesives. After completely dried under an infrared lamp, the single cell was fastened in a vertical tubular furnace. The humidified H_2 were fed to the hydrogen electrode side with a flow rate of 40 $mlmin^{-1}$, which was precisely controlled using a digital mass flow controller (APEX, Alicat Scientific). Steam at different volume fractions were generated using a humidifier, which was heated to the target temperatures. The partial water pressure was monitored using an on-line humidity sensor (HMP 337, Vaisala). Before each test, the SFMNi-SDC electrode was fully reduced in the 3 vol.% H_2O humidified H_2 atmosphere at 800 ^{o}C, open circuit voltage (OCV) was recorded until it become stable. Electrochemical measurements are performed using an electrochemical workstation (Zahner Zennium E). Current density-cell voltage (*i-V*) curves were recorded by sweeping the cell voltage from 0.4 to 1.4 V at a scanning speed of 0.03 Vs^{-1}, and electrochemical impedance spectra (EIS) were recorded in the frequency range from 1 MHz to 0.01 Hz with an amplitude of 30 mV.

The crystalline structure of synthesized powders was characterized by XRD using a D/MAX-3C X-ray diffractometer. The analysis of XRD patterns were performed using the MDI Jade 6.0 software. The microstructure and composition distribution of the reduced SFMNi-SDC hydrogen electrode were characterized by using a scanning electron microscope (SEM, Zeiss Crossbeam 540) equipped with energy dispersive X-ray spectrometers (EDS) system. The morphologies of the reduced SFMNi powders were characterized using high resolution transmission electron microscope

(HRTEM) (JEM-2100F, JEOL).

2.4 Computational methods

Since the exsolution process from M^{n+} to M^0 for ABO_3 perovskite oxide is inclined to occur under the driving force of negative Gibbs free energy change ($\Delta G<0$), in order to study the chemical stability of SFMNi materials, the thermodynamic feasibilities of metal oxides (NiO and Fe_2O_3) under different equilibrium partial oxygen pressures were analyzed by using Ellingham diagram[31].

DFT calculations were carried out using Vienna Ab Initio Simulation Package (VASP)[32, 33]. The electron exchange correction was treated with the Perdew-Burke-Ernzerhof (PBE) in the framework of generalized gradient approximation (GGA)[34]. Based on our XRD patterns and TEM images, an SFM slab model was constructed with vacuum thickness of up to 20 Å, which was sufficient to describe surface phenomena (Figure S1). The cutoff energy of 500 eV was chosen for plane wave expansion of wave functions and a 3×3×1 Monkhorst-Pack *k*-point sampling over the first Brillouin zone was employed for all slab model calculations[35]. Structures were relaxed until the atomic forces on each ionic were less than 0.02 eV/Å and the electron relaxation convergence criterion was 10^{-4} eV in two consecutive loops. And then the oxygen vacancy-formation energy (E_{vf}) and the segregation energy of B-site metal with or without oxygen vacancies were calculated.

3. Results and Discussion

3.1 Phase, structure and morphology

The phase composition of the fresh and reduced SFMNi powders is evaluated by XRD measurement, and shown in Figure 1a. It can be seen from Figure 1a that the XRD patterns of SFMNi powders calcined at 1050 ^oC show single cubic perovskite crystal structure (PDF# 34-0638),

suggesting that the doping of Fe with Ni does not alter the phase purity of the perovskite oxide. However, two extra peaks at 44 and 51° besides the characteristic XRD patterns of perovskite matrix are observed for the SFMNi materials subjected to reduction at 800 °C in 3 vol%H_2O humidified H_2 atmosphere, and these two extra peaks are identified to be indexed with taenite (PDF #47-1417), a kind of Fe-Ni alloy, which were also observed by Xiao *et al.*[18]. The perovskite oxide SFMNi powders consisting of fine Fe-Ni alloy nano-particles with a diameter of 20-30 nm are also confirmed by HRTEM image in Figure 1b. Two lattice distances of around 0.272 and 0.179 nm have been revealed, which are consistent with the 0.272 nm distance between two (110) planes of SFMNi crystalline structure (space group Pm3m) and the 0.179 nm distance between two (111) planes of Taenite crystalline structure (space group Fm3m) determined by the XRD analysis. In addition, SAED pattern for the SFMNi powders after reduced in humidified H_2 at 800 °C is collected and shown in Figure 1c. The ring pattern is carefully measured and compared with JCPDS-PDF cards. It can be found most of the circles fitted well with the SFMNi and Fe-Ni alloy respectively, consistent with XRD result (Figure 1a). These results indicate that a Fe-Ni alloy structured perovskite composite materials could be successfully prepared via in-situ reduction under the conditions similar to that in the hydrogen electrode of SOCs. Figure1d shows the morphology of SFMNi-GDC bars after reduced in humidified H_2 at 800 °C, it can be seen that a significant amount of nano-sized particles is exsolved from and homogeneously dispersed on the matrix. To further characterize the nature of the exsolved nanoparticles structured composite, EDS elemental mapping are collected and shown in Figure1e-k. The elements contributed to nano-sized particles are rich in Ni and Fe elements, but lack of O element, indicating that the exsolved nanoparticles are Fe-Ni alloy. The result is consistent with the secondary Fe-Ni alloy peaks in the XRD patterns. Moreover, the

XRD results have been refined to further determine the composite of the SFMNi powders after reduction, and the Rietveld refinement of the XRD difractogram is shown in Figure S2. All diffraction peaks could be indexed to the respective perovskite oxide and cubic Fe-Ni alloy (Taenite), with no evidence of a second phase formation. Calculations give a = 3.94407(4) Å in space group Pm3m for perovskite oxide and a = 3.55904(7) Å in space group Fm3m for cubic Fe-Ni alloy (Taenite), respectively. These data indicate that the composite of nanoparticles is Fe-Ni alloy (Taenite). Similar phenomena have been reported in Ni or other active metals doped perovskite oxide in the reducing atmosphere. For instance, Du *et al*. have observed metallic phase indexed with $FeNi_3$ alloy was formed during the reduction of perovskite $Sr_2FeMo_{0.65}Ni_{0.35}O_{6-\delta}$ materials[36], which is different from our results (Taenite) and possibly ascribed to the different perovskite parent oxide. Sun *et al.* have also reported nano-particles in the form of Ni-Fe alloy were in-situ exsolved from $(La_{0.7}Sr_{0.3})(Cr_{0.85}Ni_{0.1125}Fe_{0.0375})O_{3-\delta}$ perovskite oxide[26]. The ex-solved nano-sized metallic catalysts would not only largely improve the catalytic properties of the cathode materials but also extend the active reaction sites, and thus further enhance the electrochemical performance of the SOCs.

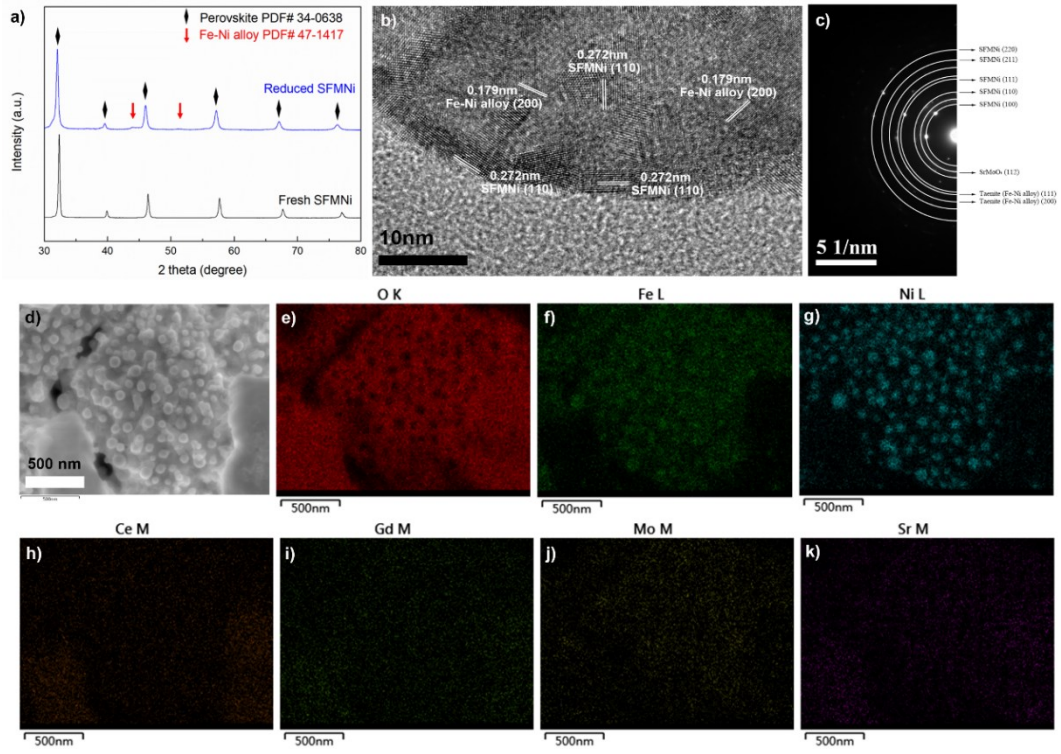

Figure 1 a) XRD patterns of the SFMNi powders before and after reduced in the 3 vol% H_2O humidified H_2 atmosphere at 800 °C for 10 hours, b) HRTEM image and c) SAED patten for the SFMNi powders after reduced in humudified H_2 at 800 °C, d) SEM images of SFMNi-GDC bars after reduced in humudified H_2 at 800 °C, and EDS elemental distribution mapping of e) O K, f) Fe L, g) Ni L, h) Ce M, i) Gd M, j)Mo M, k) Sr M edges.

3.2 *In-situ* exsolution mechanism

Figure S3 shows the Ellingham diagram of nickel oxide reaction ($2Ni_{(s)}+O_{2(g)}=NiO_{(s)}$), and the left *y*-axis represents the standard Gibbs free energy, while the right *y*-axis represents the equilibrium partial oxygen pressure, which corresponds to ΔG of zero and could be derived by extending line from the origin of the graph (T=0, ΔG=0) to the point on Ellingham line at required temperature (T, ΔG)[31]. When the practical partial pressure of oxygen is below the threshold value, the metal oxide could disassociate to form metallic phase due to the negative free energy change for metal oxide reduction reaction, otherwise, the metal oxide is thermodynamically stable. As a result, the

equilibrium partial pressure is often known as the dissociation pressure. Figure 2 shows the threshold PO_2 for the Ni and Fe metal reduction from NiO and Fe_2O_3 at temperature range from 200 to 1000 °C. At 800 °C, the threshold PO_2 for Ni and Fe metal reduction is $10^{-13.95}$ and $10^{-17.70}$ bar, respectively, below which Ni and Fe could be spontaneously formed. In conditions of 3vol% H_2O humidified H_2 atmosphere, the practical partial oxygen pressure at 800 °C is $10^{-21.38}$ bar, which is below both of the threshold PO_2 for Ni and Fe reduction. The results indicate that both of Ni and Fe could be formed from the reduction of metal oxide in thermodynamic perspective during the SOFC/SOEC operation.

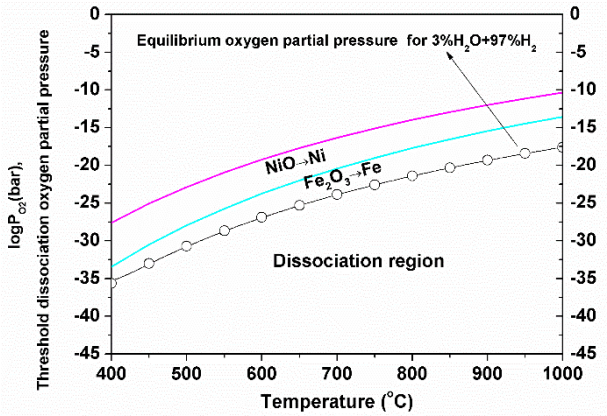

Figure 2 Threshold dissociation oxygen partial pressure for the Ni and Fe metal reduction from NiO and Fe_2O_3 at the temperature range from 200 to 1000 °C calculated by Ellingham diagram.

Kwon *et al*. have performed DFT calculations to identify the effect of co-segregation energy on exsolution during *in-situ* reduction, and found that the *in-situ* exsolution process was strongly associated with oxygen vacancies and B-site metal vacancies introduced by *in-situ* reduction[23], and utilized the oxygen vacancies formation energy, co-segregation energy and total energy of the B-site metal to clearly explain the mechanism of the *in-situ* exsolution phenomenon in layered perovskite oxides. Therefore, to better address how the in-situ exsolution phenomenon occurred in the perovskite oxide SFMNi material, a similar work based on DFT calculations has been done

(Figure 3), and the oxygen vacancies formation energy, co-segregation energy and total energy of the B-site metal were calculated and compared. Table S1 shows the calculated oxygen vacancy formation energy at each layer's lattice oxygen. The formation of oxygen vacancy in odd layers is more easily than that of oxygen vacancies in even layers. Typically, the value at the second layer lattice O site is 3.70 eV. The oxygen vacancy formation energy at the odd lattice O sites increases from the first layer (0.87 eV) to the third layer (1.70 eV), indicating that oxygen vacancies formed in the bulk prefer to be segregated out to the surface from the bulk. In addition, the total energy of SFMNi for Ni in different layers are also calculated and the relative energy is shown in Table S1. It can be seen that the total energy at the surface is lower in 0.40 eV than that in the third layer, implying that Ni element is inclined to exsolve from the bulk during the reduction. Moreover, it is also found that the co-segregation energy of Fe and Ni is -0.83 eV and -0.53 eV with oxygen vacancies, respectively (Figure 3b), demonstrating that the oxygen vacancy can promote the reduction reaction. As we all know, once the B-site metal and oxygen vacancy co-segregate towards the surface from the bulk, stabilization of the segregated phase containing B-site elements on the surface is required to maintain the B-site dopant as metallic phase. Therefore, it is expected that metallic Fe-Ni alloy nanoparticles exist on the surface of perovskite oxide SFMNi, which is in good agreement with our experimental results observed by XRD, HRTEM, SEM-EDS.

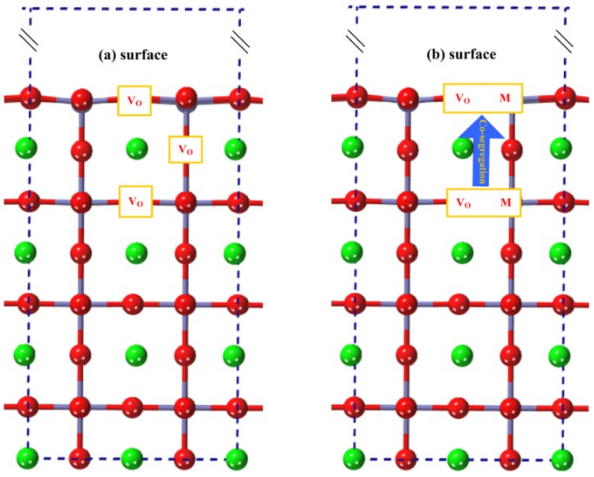

Figure 3 a) Side view of possible oxygen vacancy positions at layer's lattice oxygen for 1-3 layers, and b) Schematic illustration of our model used for the calculations of co-segregation energy. The inset boxes indicate the co-segregation of M (M=Fe, Ni) with an oxygen vacancy.

2.3 Transport properties

Figure 4a shows the electrical conductivity of reduced SFMNi-GDC and SFM-GDC bars measured in the 10%H_2-90%N_2 atmosphere from 400 to 800 °C with an interval of 50 °C. The GDC components are incorporated to prevent possible microstructural damages, resulted from volumetric shrinkage by metal exsolution during the *in-situ* reduction process. It is observed that the reduced SFM-GDC composite materials without Ni doping in the 10%H_2-90%N_2 atmosphere have a conductivity of 10.8 Scm^{-1} at 800 °C, which is comparable to other most commonly used typical perovskite-type anode materials (such as LSCNi-Fe, 1.2 Scm^{-1}@800 °C, $La_{0.75}Sr_{0.25}Cr_{0.5}Mn_{0.5}O_3$, 3 Scm^{-1}@900 °C, $(Pr_{0.4}Sr_{0.6})_3(Fe_{0.85}Nb_{0.15})_2O_{7-\delta}$, 19 Scm^{-1}@800 °C)[5, 17, 26]. The conductivity of reduced SFMNi-GDC with Ni doping has increased to 12.6 Scm^{-1}, which fulfills the requirement of conductive properties for advanced hydrogen electrode for SOCs application, and suggests sufficient electron transfer paths for the electrode reactions[36]. Furthermore, it is also noticed that the electrical conductive behavior is a thermally activated process, and $\ln\sigma T$ has a linear relationship

with $1/T$, as the small polaron conductivity equation describes,

$$\sigma = \left(\frac{A}{T}\right) exp\left(-\frac{E_a}{kT}\right). \quad (1)$$

Two different slope with the activation energy E_a of 0.332±0.12 eV and 0.257±0.007 eV are observed from 400 to 800 ºC for SFM-GDC sample, which could be explained by the fact that two different kinds of charge compensation of oxygen vacancies and electron hopping along $Fe^{2+}(Mo^{5+})$-O-$Fe^{3+}(Mo^{6+})$ bonds are responsible to the conductivity. The doping of Ni has led to a reduced E_a to 0.145±0.003 eV and 0.102±0.003 eV, which is possibly relegated to an increased concentration of oxygen vacancies. Figure 4b shows the normalized conductivity of the SFMNi-GDC and SFM-GDC bars as a function of elapsed time over the surrounding atmosphere switching from 67%CO-33%CO_2 to 50%CO-50%CO_2 at 800 ºC. It can be seen from Figure 4b that the re-equilibrium time for SFMNi-GDC bar is shorter than that for SFM-GDC bar, moreover, which is also much faster than that measured on other ceramic materials. The fitting results agree well with the measured plot at the oxygen surface exchange coefficients (k_{chem}) of 1.7×10^{-3} to 0.5×10^{-3} cms^{-1} as well as the oxygen diffusion coefficient (D_{chem}) of 3.0×10^{-5} to 6.0×10^{-5} cm^2s^{-1} for SFMNi-GDC and SFM-GDC bars, respectively. These results demonstrate that oxygen surface exchange process of SFM-based material can be greatly accelerated by the Fe-Ni alloy nanoparticles *in-situ* exsolved from SFMNi parent materials. However, the oxygen diffusion process is partially decelerated, which is possibly attributed to the decreased effective paths for oxygen ion diffusion blocked by the *in-situ* exsolved Fe-Ni alloy nanoparticles. It should be also noted that the oxygen diffusion coefficient is still comparative with the other ceramic materials[5, 17, 26]. Therefore, it can be concluded that the reduced SFMNi-GDC composite could be a promising electrode for solid oxide cells with high performance.

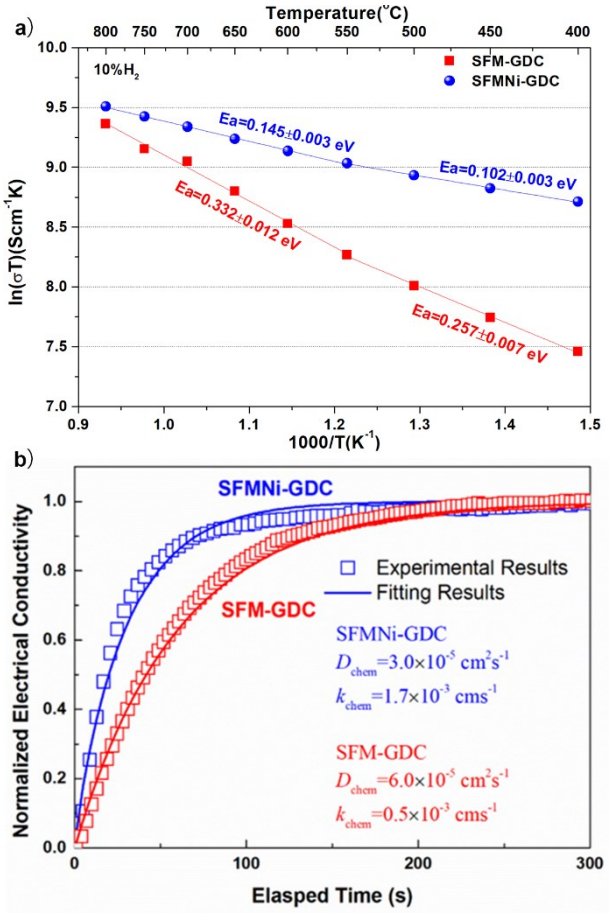

Figure 4 a) the electrical conductivity of reduced SFMNi-GDC and SFM-GDC bars measured in the 10%H_2-90%N_2 atmosphere at the temperature range of 400-800 °C, b) normalized conductivity of the SFMNi-GDC and SFM-GDC bars as a function of the elasped time over the surrounding gas switching from 33%CO_2-67%CO to 50%CO_2-50%CO at 800 °C.

2.4 Morphology and electrochemical performance of the cells

Figure 5a and 5b show the cross-sectional SEM images of SFMNi–SDC/ LDC/ LSGM/SDC–LSCF single cell. The LSGM electrolyte is about 500 μm thick and totally dense after sintering at 1400 °C, and the LDC interlayer is about 3 μm thick and well-contacted with the LSGM electrolyte to prevent the possible chemical reactions between the SFMNi-SDC hydrogen electrode and the LSGM electrolyte. The SFMNi-SDC electrode is porous with a thickness of about 34 μm, which is also well-connected to the LDC interlayer after sintering at 1100 °C. Before running the SFMNi–

SDC/LDC/LSGM/SDC–LSCF single cell, the SFMNi-SDC cathode is reduced in the 3 vol%H_2O humidified H_2 atmosphere to get metallic catalysts be fully ex-solved. Figure 5c and 5d show the SEM images of the SFMNi-SDC electrode before and after SOC test. It is revealed that nano-sized foreign particles identified as Fe-Ni alloy (Figure 1) are exsolved from the perovskite parent and uniformly anchored beneath the substrate in the diameter of 20-30 nm (Figure 5d). The nano-catalysts have large specific surface areas, which would extend active reaction sites for electrode reaction and accelerate the surface oxygen exchange process (Figure 4b), and thus helping to enhance the electrochemical performance of SOCs.

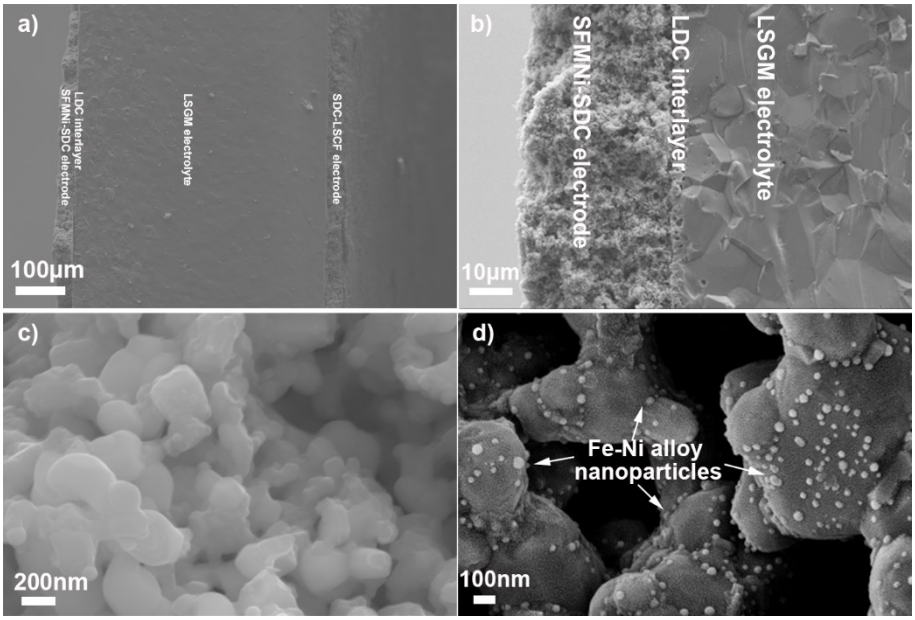

Figure 5 a-b) cross-sectional SEM images of the SFMNi–SDC/LDC/LSGM/SDC–LSCF single cell, and SEM images of the SFMNi-SDC electrode c) before and d) after SOC test.

The electrochemical performance of in-situ nano-sized Fe-Ni alloy structured SFMNi electrodes have been performed in the LSGM electrolyte-supported cells with a configuration of SFMNi-SDC/LDC/LSGM/SDC-LSCF. The effect of steam content on the cell performance is studied by varying the steam concentrate from 3% to 42% in the hydrogen electrode side, on the other side, the oxygen electrode of SDC-LSCF composite electrode is exposed to ambient air. As is shown in

Figure 6a, the current density-cell voltage (*i-V*) curves are recorded by scanning the absolute voltage from 1.5 V to 0.2 V at a sweeping rate of 30 mVs^{-1}. With the steam content increasing from 3% to 13%, 23% and 42%, the open circuit voltage (OCV) at 800 °C has be decreased from 1.04 to 1.00, 0.96 and 0.92 V, respectively. The results of reducing OCVs with increasing steam content is in accordance with Nernst equations illustrated by the following equation:

$$V_N = \frac{-\Delta G_{f,H_2O}(T)}{2F} - \frac{RT}{2F} ln\left(\frac{y_{1,H_2O}}{y_{1,H_2} y_{O_2}^{0.5}}\right) \text{ or } V_N = \frac{RT}{4F} ln\left(\frac{P_{O_2,H}}{P_{O_2,O}}\right) \quad (1)$$

The equilibrium oxygen partial pressures in the hydrogen electrode side at the different steam contents, $PO_{2,H}$, are also calculated by using the HSC 5.0 software to evaluate the theoretical Nernst potentials (V_N). The value of $PO_{2,H}$, corresponding to the atmosphere of 3%H_2O-97%H_2, 13%H_2O-87%H_2, 23%H_2O-77%H_2 and 42%H_2O-58%H_2 are 4.09×10^{-22}, 9.55×10^{-21}, 3.82×10^{-20} and 2.24×10^{-19} atm, respectively, and the corresponding theoretical Nernst potentials are calculated to be 1.10, 1.03, 1.00 and 0.96 V, which is in accordance with the trend of OCVs observed in Figure 6a. Moreover, it should be noticed in Table S2 that the theoretical Nernst potentials are close to the OCVs, indicating that the water splitting reaction has nearly reached equilibrium on the nano-sized Fe-Ni alloy structured SFM cathode. The discrepancy less than 0.06 V is possibly attributed to gas leakage or different localized gas condition from the main gas channel. Furthermore, it could also be observed that the electrochemical performance increases with increasing the steam content. In conditions of 800 °C and 1.3 V, the electrolysis current density has been increased from 437 to 636, 737 and 838 $mAcm^{-2}$ with the steam concentration increasing from 3% to 13%, 23% and 42%, respectively. Assuming no side reactions and 100% Faraday's efficiency, it could generate the hydrogen gas at a rate of 184, 267, 310 and 350 $mLcm^{-2}h^{-1}$, respectively. The increased electrolysis cell performance with increasing the steam content could be explained by the fact that higher steam

content suggests a larger reactant concentration, and consequently facilitates the water splitting reaction, $H_2O=H_2+O_2$, moving forward to produce hydrogen gas.

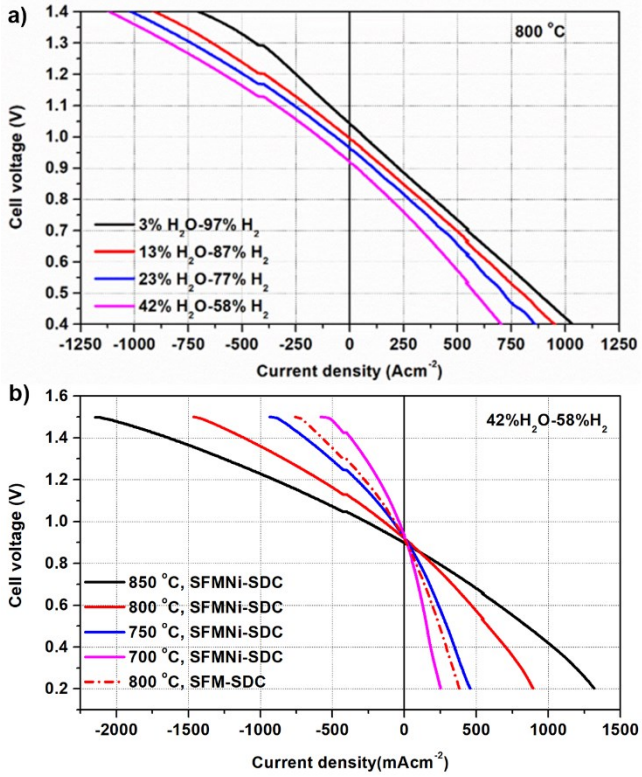

Figure 6 *i-V* curves of the SFMNi-SDC/LDC/LSGM/SDC-LSCF cell recorded as a function of a) the steam content in the hydrogen electrode, and b) the operating temperature.

The effect of operating temperature on the cell performance is also investigated in both SOFC and SOEC modes. Figure 6b shows *i-V* curves of SOCs measured at the operating temperatures from 700 to 850 °C. The in-situ nano-sized Fe-Ni alloy structured SFMNi perovskite hydrogen electrode is controlled at 42%H_2O-58%H_2 atmosphere, while the SDC-LSCF oxygen electrode is exposed to ambient air. As is shown in Figure 6b, OCV is decreased with increasing the operating temperature as expected using Nernst equations (Eq. (1)). OCVs of 0.93, 0.92, 0.92 and 0.90 V are measured at 700, 750, 800 and 850 °C, respectively, which are also very close to the theoretical values shown in Table S2. The electrochemical performance increases with the operating temperature, which is strongly ascribed to the increased conductivity of electrolyte and promoted

kinetics of electrode reactions. For instance, at the applied voltage of 1.3 V, an electrolysis current density of 269 $mAcm^{-2}$ has been achieved at 700 °C, which is increased to 511 $mAcm^{-2}$ at 750 °C, 838 $mAcm^{-2}$ at 800 °C, and further 1257 $mAcm^{-2}$ at 850 °C, respectively. The performance has been significantly improved in comparison with the SFM-SDC/LDC/LSGM/SDC-LSCF cell, which generates an electrolysis current density of 426 $mAcm^{-2}$ at 800 °C and an electrolysis voltage of 1.3V. Moreover, it should be noted that no obvious signal of concentration polarization normally featured as $d^2V/d^2i>0$ is observed in the *i-V* curves at the operating temperature from 700 to 850 °C.

The steam electrolysis performance of solid oxide cells using other different hydrogen electrodes are also summarized in Figure 7 for comparison[5, 6, 9, 13, 17, 37-39]. The *i-V* curves of SFMNi-SDC/LDC/LSGM/SDC-LSCF cells measured at 850 °C,42%H_2O-58%H_2 stay left than that of most other cells, indicating that a much higher electrolysis current density is generated at the same applied cell voltage. For SFMNi-SDC/LDC/LSGM/SDC-LSCF cells, the electrolysis current density at 1.3V, 850 °C is 1257 $mAcm^{-2}$, which is higher than 78 $mAcm^{-2}$ for LSNT/YSZ/YSZ-LSM@850 °C,47% H_2O-53% N_2[9], 244 $mAcm^{-2}$ for LSCM-YSZ/YSZ/LSM-YSZ@850 °C, 40%H_2O-60%H_2[5], 300 $mAcm^{-2}$ for Ni-YSZ/YSZ/LSM-YSZ@800 °C, 50% H_2O-50% H_2[39], 526 $mAcm^{-2}$ for SFM/LSGM/SFM@850 °C, 40% H_2O-60% H_2[6], 639 $mAcm^{-2}$ for SFM-SDC/LDC/LSGM/SDC-LSCF@850 °C, 42% H_2O-58% H_2[13], 979 $mAcm^{-2}$ for K-PSCFN-CFA/LSGM/BCFN@850 °C,40% H_2O-60% H_2[17], even comparable to 1355 $mAcm^{-2}$ for the phase-inversion tape casting Ni-YSZ/YSZ/YSZ-LSM@800 °C,33% H_2O-67% H_2 [38]. The excellent electrochemical performance of in-situ fabricated nano-sized Fe-Ni alloy structured SFM electrode could be mainly attributed to the high catalytic activity of Fe-Ni alloy nano-catalyst toward steam splitting reaction.

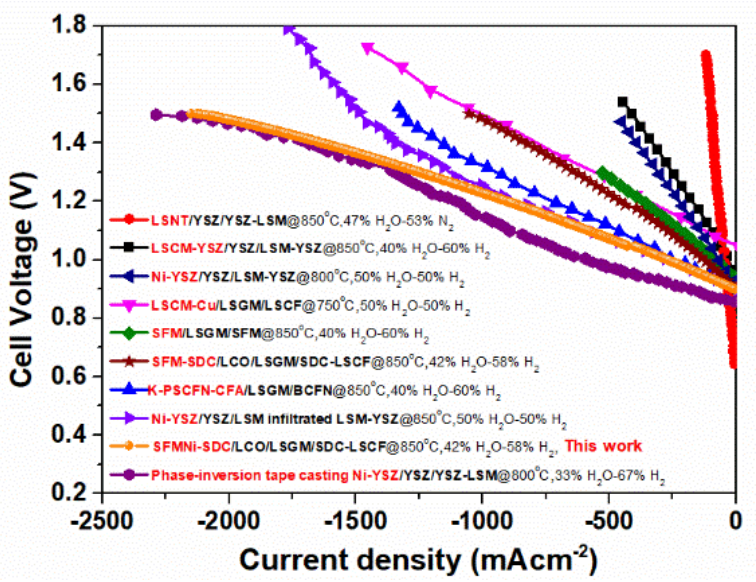

Figure 7 Steam electrolysis performance of solid oxide cells using different hydrogen electrodes reported in the literatures.

Impedance spectra for solid oxide electrolysis cell comprised of SFMNi-SDC/LDC/LSGM/SDC-LSCF are measured at OCV from 700 to 850 °C to further understand the electrode reaction process. These in-situ nano-sized Fe-Ni particles structured SFMNi perovskite electrode is operated in conditions of 42%H_2O-58%H_2, while the SDC-LSCF electrode is exposed to ambient air. As is shown from the Nyquist plots in Figure 8a, the first *x*-intercept describes the ohmic resistance, R_{ohm}, which is mainly attributed to the electrolyte and the contact between electrolyte and electrode. At 700 °C, the LSGM-supported solid oxide electrolyzer has an ohmic resistance of 0.5 Ωcm^2, which is close to the theoretical value of the LSGM electrolyte as evaluated from its ionic conductivity. The result indicates that the electrolyte and the electrode are well connected, which is strongly in accordance with the morphology shown in the SEM image (Figure 5). The ohmic resistance has decreased to 0.35, 0.24 and 0.19 Ωcm^2 at 750, 800 and 850 °C, respectively, because of an increased ionic conductivity of the electrolyte. The electrode polarization resistance is measured to be 1.38, 0.71, 0.35 and 0.20 Ωcm^2 at 700, 750, 800 and 850 °C, respectively, which is decreased by the

improved catalytic activities of the electrodes. Distribution of relaxation time (DRT) analysis are also used to distinguish the overlapping arcs of impedance spectra[40-44], where each peak corresponds to some of the key sub-steps involved in the electrode reactions. The integral area of the peak represents the polarization resistance of the sub-step. The characteristic frequency of the peak is inversely proportion to the relaxation time of the sub-step, the higher the characteristic frequency, the faster the relaxation of the sub-step. It is observed in Figure 8b that four to five peaks are identified over the frequency range of 10^{4}~10^{-2} Hz. However, three main integral area contributed to the total electrode polarization resistance, consequently, a simplified three-element equivalent circuit model R(QR)(QR)(QR) is created to simulate the impedance spectra. The original data are fitted well to the equivalent circuit model with a standard deviation less than 5%. Moreover, it should be noticed that the intermediate peaks located at 2~10 Hz are the rate-limiting steps, which has been effectively accelerated by increasing the operating temperature. Yan *et al.* has summarized the impedance spectra distribution pattern for solid oxide steam electrolysis cells[45], and found that the middle frequency arc at about 10 Hz are commonly attributed to the gas conversion process at the hydrogen electrode. Nechache *et al.* has assigned the arc with characteristic frequency of 10 Hz to H_2O diffusion while the arc at 1 Hz to H_2O gas conversion[46]. Therefore, it can be concluded that gas conversion process in the SFMNi-SDC hydrogen electrode is the rate-limiting step, implying that the cell performance can be further enhanced by accelerating the gas conversion process in the hydrogen electrode.

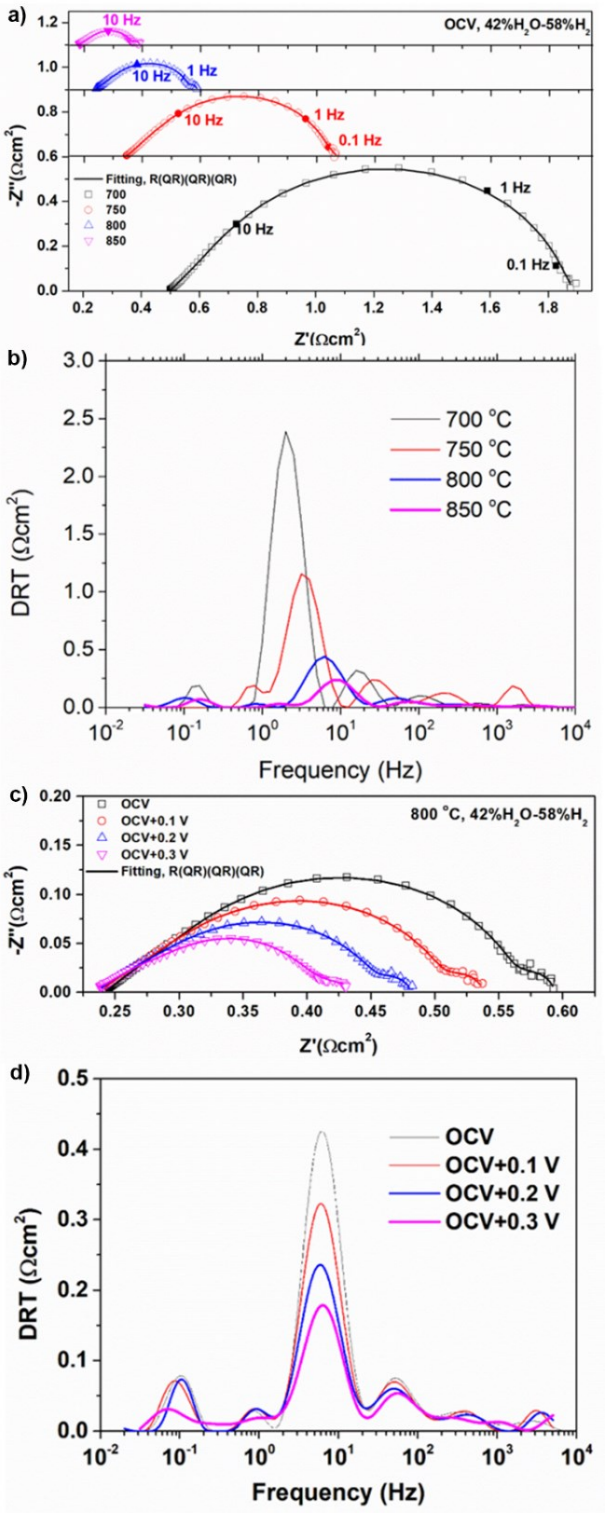

Figure 8 Typical impedance spectra and DRT results of the SFMNi-SDC/LDC/LSGM/SDC-LSCF cell recorded in the condition of 42%H_2O-58%H_2 and 800 °C as a function of a-b) the operating temperature, and c-d) the applied cell voltage.

Figure 8c shows the effects of the applied cell voltage on the impedance spectra measured in

conditions of 42%H_2O-58%H_2 and 800 °C. The ohmic resistance of the SFMNi-SDC/LDC/LSGM/SDC-LSCF cell is about 0.24 Ωcm^2 at the applied voltage of 0, 0.1, 0.2 and 0.3 V over OCV. It seems that the ohmic resistance is not affected by the increase of the applied cell voltage, indicating that none of detectible material decomposition or microstructure crack in the cell voltage range from OCV to OCV+0.3 V. At the same time, the electrode polarization resistance is measured to be 0.347, 0.293, 0.242 and 0.190 Ωcm^2 at the applied voltage of OCV, OCV+0.1, OCV+0.2 and OCV+0.3 V, respectively. The electrode polarization resistance decreases with the increase of applied cell voltage, showing a good agreement with the reduced slope of *i-V* curve in Figure 6. The results have indicated that the electrode process is accelerated under the drive of the applied cell voltage. Figure 8c and Figure 8d show the Nyquist plots and DRT analysis results for SFMNi-SDC/LDC/LSGM/SDC-LSCF cells, respectively. It can be seen that five to six peaks are identified over the frequency range of 10^4~10^{-2} Hz. The peaks located at 6, 0.1 and 50 Hz are mainly contributed to the total electrode reaction. In addition, the original data are fitted well to the equivalent circuit model R(QR)(QR)(QR). The effects of the applied cell voltage on individual arcs are also studied in the DRT curves, it is observed that the intermediate arc at 6 Hz are sensitive to the applied cell voltage, while the other two arcs at 0.1 and 50 Hz remain almost unchanged. The increase in the applied cell voltage leads to a significant decrease of intermediate peak area, thus a reduced polarization resistance, indicating that it is a sub-step activated by the applied cell voltage. Ebbesen *et al.* has evaluated the polarization resistance caused by gas conversion in H_2O-H_2 mixture using the following equation[3]:

$$R_{Conversion} = \frac{\eta_c}{i}\frac{RT}{4F^2 J_i}\left(\frac{1}{X_{i,H_2O}} + \frac{1}{X_{i,H_2}}\right) \quad (3)$$

It can be found from Eq. (3) that the increase of current, *i*, which can be achieved by increasing the

applied cell voltage, will lead to a decrease of gas conversion polarization resistance.

4. Conclusions

In the present work, self-grown metallic Fe-Ni alloy nanoparticles are fabricated from $Sr_2Fe_{1.3}Ni_{0.2}Mo_{0.5}O_{6-\delta}$ by annealing the perovskite oxide in 3 vol.% H_2O humidified H_2 atmosphere. According to the Ellingham diagram, it is feasible to occur when the practical condition is located in the disassociation region with the equilibrium oxygen partial pressure below the threshold value. XRD patterns, EDS mapping for elements and HRTEM results have confirmed the exsolution of Fe, Ni nanoparticles, which are uniformly distributed onto the perovskite oxide parent, which is also explained by DFT results. The composite combined with GDC perform sufficient electrical conductivity and attractive oxygen surface exchange coefficient. Solid oxide cells using in-situ reduced SFMNi-SDC cathode has achieved an electrolysis current density of 1257 $mAcm^{-2}$ at 1.3 V and 850 ^oC in 42%H_2O-58%H_2 atmosphere. DRT analysis of impedance spectra show that the total electrode reaction is possibly dominated by the gas conversion process, which could be accelerated by increasing the operating temperature or applied cell voltage.

Acknowledgements

The authors greatly acknowledge the financial support by Natural Science Foundation of China (grant numbers 51502207, 51602228, 21673062, 11764019), Natural Science Foundation of Jiangsu Province of China (grant number BK20160380), Natural Science Foundation of Hubei Province of China (grant numbers 2016CFB243, 2017CFB655), and the China Postdoctoral Science Foundation (grant numbers 2016M590712, 2017T100575), and the U.S. National Science Foundation (grant

number 1832809).

The authors gratefully acknowledge Dr. Wei He in Hong Kong Polytechnic University for the Rietveld refinement of the XRD data.

References

[1] L. Bi, S. Boulfrad, E. Traversa, Steam electrolysis by solid oxide electrolysis cells (SOECs) with proton-conducting oxides, Chem. Soc. Rev. 43 (2014) 8255-8270. https://doi.org/10.1039/C4CS00194J.

[2] M.A. Laguna-Bercero, Recent advances in high temperature electrolysis using solid oxide fuel cells: A review, J. Power Sources 203 (2012) 4-16. https://doi.org/10.1016/j.jpowsour.2011.12.019.

[3] S.D. Ebbesen, S.H. Jensen, A. Hauch, M.B. Mogensen, High temperature electrolysis in alkaline cells, solid proton conducting cells, and solid oxide cells, Chem. Rev. 114 (2014) 10697-10734. https://doi.org/10.1021/cr5000865.

[4] Y. Wang, C. Xia, Nano-structural effect on SOFC durability, in: D.Y.C. Leung, J. Xuan (Eds.) Micro & Nano-Engineering of Fuel Cells, CRC Press, Leiden, 2015, pp. 181-210.

[5] C. Jin, C. Yang, F. Zhao, D. Cui, F. Chen, $La_{0.75}Sr_{0.25}Cr_{0.5}Mn_{0.5}O_3$ as hydrogen electrode for solid oxide electrolysis cells, Int. J. Hydrogen Energy 36 (2011) 3340-3346. https://doi.org/10.1016/j.ijhydene.2010.12.085.

[6] Q. Liu, C. Yang, X. Dong, F. Chen, Perovskite $Sr_2Fe_{1.5}Mo_{0.5}O_{6-\delta}$ as electrode materials for symmetrical solid oxide electrolysis cells, Int. J. Hydrogen Energy 35 (2010) 10039-10044. https://doi.org/10.1016/j.ijhydene.2010.08.016.

[7] Q. Liu, X. Dong, G. Xiao, F. Zhao, F. Chen, A novel electrode material for symmetrical SOFCs, Adv. Mater. 22 (2010) 5478-5482. https://doi.org/10.1002/adma.201001044.

[8] S. Tao, J.T.S. Irvine, Synthesis and characterization of $(La_{0.75}Sr_{0.25})Cr_{0.5}Mn_{0.5}O_{3-\delta}$, a redox-stable, efficient perovskite anode for SOFCs, J. Electrochem. Soc. 151 (2004) A252-A259. https://doi.org/10.1149/1.1639161.

[9] G. Tsekouras, D. Neagu, J.T.S. Irvine, Step-change in high temperature steam electrolysis performance of perovskite oxide cathodes with exsolution of B-site dopants, Energ. Environ. Sci. 6 (2013) 256-266. https://doi.org/10.1039/C2EE22547F.

[10] D. Neagu, E.I. Papaioannou, W.K.W. Ramli, D.N. Miller, B.J. Murdoch, H. Menard, A. Umar, A.J. Barlow, P.J. Cumpson, J.T.S. Irvine, I.S. Metcalfe, Demonstration of chemistry at a point through restructuring and catalytic activation at anchored nanoparticles, Nat. Commun. 8, 1855. https://doi.org/10.1038/s41467-017-01880-y.

[11] B. Hua, M. Li, Y.F. Sun, J.H. Li, J.L. Luo, Enhancing perovskite electrocatalysis of solid oxide cells through controlled exsolution of nanoparticles, ChemSusChem 10 (2017) 3333-3341. https://doi.org/10.1002/cssc.201700936.

[12] C.C. Duan, R.J. Kee, H.Y. Zhu, C. Karakaya, Y.C. Chen, S. Ricote, A. Jarry, E.J. Crumlin, D. Hook, R. Braun, N.P. Sullivan, R. O'Hayre, Highly durable, coking and sulfur tolerant, fuel-flexible protonic ceramic fuel cells, Nature 557 (2018) 217-222. https://doi.org/10.1038/s41586-018-0082-6.

[13] Y. Wang, T. Liu, M. Li, C. Xia, B. Zhou, F. Chen, Exsolved Fe–Ni nano-particles from $Sr_2Fe_{1.3}Ni_{0.2}Mo_{0.5}O_6$ perovskite oxide as a cathode for solid oxide steam electrolysis cells, J. Mater. Chem. A 4 (2016) 14163-14169. https://doi.org/10.1039/C6TA06078A.

[14] H. Tanaka, M. Uenishi, M. Taniguchi, I. Tan, K. Narita, M. Kimura, K. Kaneko, Y. Nishihata, J. Mizuki, The intelligent catalyst having the self-regenerative function of Pd, Rh and Pt for automotive emissions control, Catal. Today 117 (2006) 321-328. https://doi.org/10.1016/j.cattod.2006.05.029.

[15] K. Zhu, T. Wu, M. Li, R. Lu, X. Zhu, W. Yang, Perovskites decorated with oxygen vacancies and

Fe–Ni alloy nanoparticles as high-efficiency electrocatalysts for the oxygen evolution reaction, J. Mater. Chem. A 5 (2017) 19836-19845. https://doi.org/10.1039/C7TA05404A.

[16] T. Zhu, H.E. Troiani, L.V. Mogni, M. Han, S.A. Barnett, Ni-substituted $Sr(Ti,Fe)O_3$ SOFC anodes: achieving high performance via metal alloy nanoparticle exsolution, Joule 2 (2018) 478-496. https://doi.org/10.1016/j.joule.2018.02.006.

[17] C. Yang, Z. Yang, C. Jin, M. Liu, F. Chen, High performance solid oxide electrolysis cells using $Pr_{0.8}Sr_{1.2}(Co,Fe)_{0.8}Nb_{0.2}O_{4+\delta}$–Co–Fe alloy hydrogen electrodes, Int. J. Hydrogen Energy 38 (2013) 11202-11208. https://doi.org/10.1016/j.ijhydene.2013.06.086.

[18] G. Xiao, S. Wang, Y. Lin, Z. Yang, M. Han, F. Chen, Ni-doped $Sr_2Fe_{1.5}Mo_{0.5}O_{6-\delta}$ as anode materials for solid oxide fuel cells, J. Electrochem. Soc. 161 (2014) F305-F310. https://doi.org/ 10.1149/2.061403jes.

[19] L. Thommy, O. Joubert, J. Hamon, M.-T. Caldes, Impregnation versus exsolution: Using metal catalysts to improve electrocatalytic properties of LSCM-based anodes operating at 600 °C, Int. J. Hydrogen Energy 41 (2016) 14207-14216. https://doi.org/10.1016/j.ijhydene.2016.06.088.

[20] B.H. Park, G.M. Choi, Ex-solution of Ni nanoparticles in a $La_{0.2}Sr_{0.8}Ti_{1-x}Ni_xO_{3-\delta}$ alternative anode for solid oxide fuel cell, Solid State Ionics 262 (2014) 345-348. https://doi.org/10.1016/j.ssi.2013.10.016.

[21] D. Neagu, G. Tsekouras, D.N. Miller, H. Menard, J.T. Irvine, In situ growth of nanoparticles through control of non-stoichiometry, Nat. Chem. 5 (2013) 916-923. https://doi.org/10.1038/nchem.1773.

[22] D. Neagu, T.-S. Oh, D.N. Miller, H. Ménard, S.M. Bukhari, S.R. Gamble, R.J. Gorte, J.M. Vohs, J.T.S. Irvine, Nano-socketed nickel particles with enhanced coking resistance grown in situ by redox exsolution, Nat. Commun. 6, 8120. https://doi.org/10.1038/ncomms9120.

[23] O. Kwon, S. Sengodan, K. Kim, G. Kim, H.Y. Jeong, J. Shin, Y.-W. Ju, J.W. Han, G. Kim, Exsolution trends and co-segregation aspects of self-grown catalyst nanoparticles in perovskites, Nat. Commun. 8, 15967. https://doi.org/10.1038/ncomms15967.

[24] S. Liu, Q. Liu, X.-Z. Fu, J.-L. Luo, Cogeneration of ethylene and energy in protonic fuel cell with an efficient and stable anode anchored with in-situ exsolved functional metal nanoparticles, Appl. Catal. B-Environ. 220 (2018) 283-289. https://doi.org/10.1016/j.apcatb.2017.08.051.

[25] Y. Li, B. Hu, C. Xia, W.Q. Xu, J.P. Lemmon, F. Chen, A novel fuel electrode enabling direct CO_2 electrolysis with excellent and stable cell performance, J. Mater. Chem. A 5 (2017) 20833-20842. https://doi.org/10.1039/C7TA05750D.

[26] Y.F. Sun, Y.Q. Zhang, J. Chen, J.H. Li, Y.T. Zhu, Y.M. Zeng, B.S. Amirkhiz, J. Li, B. Hua, J.L. Luo, New opportunity for in situ exsolution of metallic nanoparticles on perovskite parent, Nano Lett. 16 (2016) 5303-5309. https://doi.org/10.1021/acs.nanolett.6b02757.

[27] C. Yang, Z. Yang, C. Jin, G. Xiao, F. Chen, M. Han, Sulfur-tolerant redox-reversible anode material for direct hydrocarbon solid oxide fuel cells, Adv. Mater. 24 (2012) 1439-1443. https://doi.org/10.1002/adma.201104852.

[28] Y. Gao, D. Chen, M. Saccoccio, Z. Lu, F. Ciucci, From material design to mechanism study: Nanoscale Ni exsolution on a highly active A-site deficient anode material for solid oxide fuel cells, Nano Energy 27 (2016) 499-508. https://doi.org/10.1016/j.nanoen.2016.07.013.

[29] Y. Wang, J. Xu, X. Meng, T. Liu, F. Chen, Ni infiltrated $Sr_2Fe_{1.5}Mo_{0.5}O_{6-\delta}$-$Ce_{0.8}Sm_{0.2}O_{1.9}$ electrode for methane assisted steam electrolysis process, Electrochem. Commun. 79 (2017) 63-67. https://doi.org/10.1016/j.elecom.2017.04.018.

[30] B.B. Hu, Y.L. Wang, Z.Y. Zhu, C.R. Xia, H.J.M. Bouwmeester, Measuring oxygen surface exchange

kinetics on mixed-conducting composites by electrical conductivity relaxation, J. Mater. Chem. A 3 (2015) 10296-10302. https://doi.org/10.1039/C5TA00510H.

[31] https://www.doitpoms.ac.uk/tlplib/ellingham_diagrams/interactive.php.

[32] G. Kresse, J. Furthmuller, Efficient iterative schemes for ab initio total-energy calculations using a plane-wave basis set, Phys. Rev. B 54 (1996) 11169-11186. https://doi.org/10.1103/PhysRevB.54.11169.

[33] G. Kresse, D. Joubert, From ultrasoft pseudopotentials to the projector augmented-wave method, Phys. Rev. B 59 (1999) 1758-1775. https://doi.org/10.1103/PhysRevB.59.1758.

[34] J.P. Perdew, K. Burke, M. Ernzerhof, Generalized gradient approximation made simple, Phys. Rev. Lett. 77 (1996) 3865-3868. https://doi.org/10.1103/PhysRevLett.77.3865.

[35] H.J. Monkhorst, J.D. Pack, Special points for Brillouin-zone integrations, Phys. Rev. B 13 (1976) 5188-5192. https://doi.org/10.1103/PhysRevB.13.5188.

[36] Z. Du, H. Zhao, S. Yi, Q. Xia, Y. Gong, Y. Zhang, X. Cheng, Y. Li, L. Gu, K. Swierczek, High-performance anode material $Sr_2FeMo_{0.65}Ni_{0.35}O_{6-\delta}$ with in situ exsolved nanoparticle catalyst, ACS Nano, 10 (2016) 8660-8669. https://doi.org/10.1021/acsnano.6b03979.

[37] R. Xing, Y. Wang, Y. Zhu, S. Liu, C. Jin, Co-electrolysis of steam and CO_2 in a solid oxide electrolysis cell with $La_{0.75}Sr_{0.25}Cr_{0.5}Mn_{0.5}O_{3-\delta}$–Cu ceramic composite electrode, J. Power Sources 274 (2015) 260-264. https://doi.org/10.1016/j.jpowsour.2014.10.066.

[38] T. Liu, Y. Wang, Y. Zhang, S. Fang, L. Lei, C. Ren, F. Chen, Steam electrolysis in a solid oxide electrolysis cell fabricated by the phase-inversion tape casting method, Electrochem. Commun. 61 (2015) 106-109. https://doi.org/10.1016/j.elecom.2015.10.015.

[39] C. Yang, C. Jin, A. Coffin, F. Chen, Characterization of infiltrated $(La_{0.75}Sr_{0.25})_{0.95}MnO_3$ as oxygen

electrode for solid oxide electrolysis cells, Int. J. Hydrogen Energy 35 (2010) 5187-5193. https://doi.org/10.1016/j.ijhydene.2010.03.049.

[40] Y.X. Zhang, Y. Chen, M. Li, M.F. Yan, M. Ni, C.R. Xia, A high-precision approach to reconstruct distribution of relaxation times from electrochemical impedance spectroscopy, J. Power Sources 308 (2016) 1-6. https://doi.org/10.1016/j.jpowsour.2016.01.067.

[41] Y.X. Zhang, Y. Chen, M.F. Yan, F.L. Chen, Reconstruction of relaxation time distribution from linear electrochemical impedance spectroscopy, J. Power Sources 283 (2015) 464-477. https://doi.org/10.1016/j.jpowsour.2015.02.107.

[42] A. Leonide, V. Sonn, A. Weber, E. Ivers-Tiffee, Evaluation and modeling of the cell resistance in anode-supported solid oxide fuel cells, J. Electrochem. Soc. 155 (2008) B36-B41. https://doi.org/10.1149/1.2801372.

[43] Y. Chen, Y.F. Bu, Y.X. Zhang, R.Q. Yan, D. Ding, B.T. Zhao, S.Y. Yoo, D. Dang, R.Z. Hu, C.H. Yang, M.L. Liu, A highly efficient and robust nanofiber cathode for solid oxide fuel cells, Adv. Energy Mater. 7, 1601890. https://doi.org/10.1002/aenm.201601890.

[44] Y. Chen, Y. Chen, D. Ding, Y. Ding, Y. Choi, L. Zhang, S. Yoo, D.C. Chen, B. Deglee, H. Xu, Q.Y. Lu, B.T. Zhao, G. Vardar, J.Y. Wang, H. Bluhm, E.J. Crumlin, C.H. Yang, J. Liu, B. Yildiz, M.L. Liu, A robust and active hybrid catalyst for facile oxygen reduction in solid oxide fuel cells, Energ. Environ. Sci. 10 (2017) 964-971. https://doi.org/10.1039/C6EE03656B.

[45] J.B. Yan, H. Chen, E. Dogdibegovic, J.W. Stevenson, M.J. Cheng, X.D. Zhou, High-efficiency intermediate temperature solid oxide electrolyzer cells for the conversion of carbon dioxide to fuels, J. Power Sources 252 (2014) 79-84. https://doi.org/10.1016/j.jpowsour.2013.11.047.

[46] A. Nechache, M. Cassir, A. Ringuede, Solid oxide electrolysis cell analysis by means of

electrochemical impedance spectroscopy: A review, J. Power Sources 258 (2014) 164-181. https://doi.org/10.1016/j.jpowsour.2014.01.110.